nature geoscience

SUPPLEMENTARY INFORMATION

DOI: 10.1038/NGEO2622

Massive and prolonged deep carbon emissions associated with continental rifting

Hyunwoo Lee, James D. Muirhead, Tobias P. Fischer, Cynthia J. Ebinger, Simon A. Kattenhorn, Zachary D. Sharp and Gladys Kianji

Definition of tectonic degassing

The term tectonic degassing was coined by ref. 1, and can be used to differentiate mantle-derived CO_2 degassing at active volcanic centers (e.g., composite volcanoes, caldera complexes) from areas that are not directly affected by volcanism at the surface. CO_2 released from tectonic degassing is sourced from the mantle (e.g., Apennines, Italy; ref. 2) and ascends the crust through fault networks before reaching the surface in areas away from any observable volcanoes. Therefore, three specific criteria must be met under a tectonic degassing model: (1) the CO_2 must have a magmatic (mantle-derived) signature; (2) the CO_2 must ascend through the crust along faults and fractures; and (3) the CO_2 must reach the surface away from volcanic centers (e.g., composite volcanoes).

Definition of structural zones from field-based analyses and aerial mapping

We observed the highest CO_2 flux in the vicinity of faults, in a zone extending outward from the base of the fault scarp over a distance equal to the fault throw (*fault zone* in Figs. S3, S4, and Fig. 3 of the main text). Permeable sediments in faulted grabens also exhibited higher flux values than those observed in impermeable lavas in uplifted footwalls. Based on these observations, we subdivided all CO_2 flux measurements into three categories based on sample location relative to fault structure and surface geology. These structural categories include: (1) *fault zones*, defined as the area directly adjacent to the fault scarp and extending outward on the downthrown side of the fault to a distance equal to the maximum throw; (2) *hanging walls*, the downthrown side of the fault excluding the fault zone and characterized by sedimentary fill; and (3) *footwalls*, the uplifted

© 2016 Macmillan Publishers Limited. All rights reserved.

side of the fault comprising primarily rift lavas with a thin veneer of sediments in places (Fig. S4).

Structural controls on CO_2 degassing

Categorizing flux measurements into the three zones outlined above revealed distinct distributions in diffuse CO_2 flux data (Fig. S4, Table S2, and Fig. 3 of the main text). Measurements in fault zones exhibited 2 to 17 times greater mean CO_2 flux than background values recorded in the hanging walls and footwalls of faults (Table S2). Furthermore, mean flux values in the permeable sediment fill in downthrown hanging walls were 5 to 11 times greater than mean flux in impermeable rift lavas in uplifted footwalls. Consistent with previous studies of diffuse CO_2 flux in tectonically active regions[3], these results imply a structural control on the flux of CO_2 through the Magadi-Natron basin. High CO_2 flux occurred near the base of fault scarps, suggesting focused flow of CO_2-rich fluids through fault structures with high crustal permeability[1], which is further supported by observations of aligned spring systems at the base of some fault scarps (Table S4, and Fig. 3 of the main text). Faults in the Magadi-Natron basin form as dilational normal faults[4,5], which produce fault-related apertures in the near the surface (<500 m depth: ref. 6) that likely facilitate diffuse CO_2 transport into overlying sediments. In the shallow subsurface, CO_2 spreads diffusely throughout these permeable sediments in the hanging wall of the fault (for example, ref. 3), with negligible flux occurring through impermeable rift lavas in the uplifted footwall (Fig. S4, Table S2, and Fig. 3 of the main text).

Estimating CO_2 flux in the Magadi-Natron basin and Eastern rift of the EAR

Although CO_2 gas emits diffusely over the 982 km^2 study area in the Magadi-Natron basin, there are clear differences in flux within the three structural zones defined above (Fig. S4 and Table S2). To account for these observed variations, we calculate total flux within each of our defined zones

© 2016 Macmillan Publishers Limited. All rights reserved.

by multiplying the area of each zone (Fig. S3 and Table S3) by its mean CO_2 flux (Table S2). These values are then summed to calculate total diffuse CO_2 flux in the study area (Table S3). The areas occupied by downthrown graben sediments and uplifted trachyte lavas on the hanging walls and footwalls of faults, as well as fault traces (Fig. S3), were mapped from aerial photography (0.5 m resolution), Landsat 7 false color imagery (15 m resolution) and the Aster GDEM v.2 (30 m resolution), and validated in the field. Applying the method of ref. 7, fault throw (T) was estimated from the throw-length scaling relationship within the Magadi-Natron fault population using $T = \gamma L$ (Eq. 1), where L is fault length and γ is the throw/length coefficient. Our study used a γ of 0.0061 for faults of the Magadi-Natron basin, which was estimated from 30 faults measured from the Aster GDEM v.2 and aerial photography (0.5 m resolution). This value of γ is similar to dilation normal fault systems forming in rift lavas in Iceland (0.006; ref. 5). The area of the fault zone for each fault was then calculated by multiplying the fault length by fault throw calculated using equation 1.

Uncertainties in our flux estimates are reported as the standard error of the sample distributions (Tables S2, S3). Previous field studies of diffuse CO_2 degassing used a densely-sampled grid over comparatively smaller areas, collecting ~10-100 samples per km^2 (ref. 8, 9) compared to ~1 per km^2 collected for this work. However, our study area is 1 to 2 orders of magnitude larger than those of previous studies and was, therefore, comparatively sparsely sampled (565 measurements over 982 km^2). The diffuse CO_2 flux is also clearly influenced by fault structure and permeability of the substrate (Fig. S4). These two factors limit the application of existing methods of geostatistical analysis (for example SGeMS) used to quantify total CO_2 flux[8-10]. For these reasons, we suggest that the "structural-area method" outlined in the section above (Table S3) currently provides the most robust estimate of total CO_2 flux for the study site. It is, however, challenging

© 2016 Macmillan Publishers Limited. All rights reserved.

to estimate the extent to which our collected flux data represents a fair distribution of CO_2 flux in the defined structural zones. We have therefore used a conservative estimate of total flux across the entire Magadi-Natron basin. Essentially, we calculated a CO_2 flux of 4.05 Mt yr^{-1} over only ~10% of the 9,200 km^2 Magadi-Natron basin (combined study area = 982 km^2; Fig. S3 and Table S3), but conservatively assumed that this amount represents the total flux across the entire Magadi-Natron basin. In this study, the basin length is defined as the distance from Oldoinyo Lengai to Suswa volcano (184 km long), and basin width is defined as the distance from the western border fault system to the eastern edge of the faulted monoclinal flexure in the hanging wall of the half-graben structure (50 km wide; ref. 11). Assuming a total CO_2 flux of 4.05 Mt yr^{-1} for the 9,200 km^2 Magadi-Natron basin equates to a minimum value of flux per unit area of 4.4×10^2 t km^{-2} yr^{-1}. This conservative value is one to two orders of magnitude lower than typical flux per unit area estimates of tectonic degassing in smaller (~10^1 km^2), geothermal regions elsewhere[12], yet the total flux is significant compared to flux values from historically active volcanoes (Fig. S5).

The minimum CO_2 flux calculated for the Magadi-Natron basin may be used to extrapolate an estimate of CO_2 flux for the entire Eastern rift of the EAR. We applied rift dimensions in accordance with ref. 13, and define the Eastern rift to include rift basins from the Afar depression southward to the Kilombero rift over a total area of 3,240 × 50 km. By extrapolating CO_2 flux per unit area from the Magadi-Natron basin (4.4×10^2 t km^{-2} yr^{-1}) across the Eastern rift, we make a number of assumptions about the nature of magmatism, faulting, and fluid migration in this rift sector. First, we assume that strain accommodation proceeds in a similar manner across the Eastern rift via dike intrusion and faulting. Second, plate spreading is accommodated across the full width of rift basins, as suggested by the distribution of seismicity observed across the Eastern rift[14-19] (Fig. 1 of the main text). Third, we assume that the faulted basins are underlain by zones of magma

© 2016 Macmillan Publishers Limited. All rights reserved.

intrusion, as detected in geophysical imaging, and detection of active intrusions[14,15,19-23,]. Fourth, we assume that fluids exsolved from these crustal and upper mantle magma bodies migrate through permeable fault zones, which is supported by fluid-driven lower crustal and upper mantle earthquakes observed in the Albertine rift basin[24] and in magmatic rifts elsewhere (e.g., Taupo Rift, New Zealand; ref. 25).

Sources of CO_2 in the Magadi-Natron basin

CO_2 is removed from the mantle by the generation and ascent of magma. It exsolves from magma during cooling, crystallization and decompression, before rising through lithosphere along fractured, permeable pathways[1, 26]. Seismic and magnetotelluric studies along the Eastern rift provide evidence for volumetrically significant accumulations of magma at depth[14-15, 20-23, 27-29]. This magma is the likeliest source of the mantle-derived CO_2 measured at the surface. Here we discuss the possible location of the source (upper crust, lower crust, or upper mantle) in the Magadi-Natron basin based on previous work and the lower crustal seismicity presented in this study.

Upper crust. Although two shallow dike intrusions (< 10 km deep) have been detected by InSAR and temporary seismic arrays in the Magadi-Natron basin in the last 20 years[14, 17, 30], the volume of these intrusions is too small to supply the estimated 4.05 Mt yr^{-1} of CO_2. For example, assuming that the 2.4 m-wide, 7 km-long and 4 km-high 2007 Natron dike[21, 30] consisted of 1 wt% CO_2 and had a density of 3000 kg m^{-3}, it would have sourced only 2 Mt of CO_2 to the Magadi-Natron basin 7 years prior to the current survey. Based on analogy to other rift sectors (e.g., Main Ethiopian Rift; ref. 15, 23), the primary CO_2 is thus likely sourced from lower crustal and mantle lithosphere magma bodies.

© 2016 Macmillan Publishers Limited. All rights reserved.

Lower crust and Upper mantle. Anomalously low uppermost mantle (Pn) velocities across the Magadi sector of the Kenya Rift can be explained by a zone of ~5% partial melt[20, 22]. CO_2 may exsolve from magmas in the partial melt zone, and then travel vertically through faults in a strong, mafic lower crust, resulting in the observed deep seismicity (e.g., ref. 24, 31). Alternatively, lower crustal seismicity could also be caused by active magma intrusion[15] and volatile-driven hydraulic fracturing along the margins of modern dike and sill intrusions[32], or in some places represent detachment faulting[33].

© 2016 Macmillan Publishers Limited. All rights reserved.

Supplementary Figures

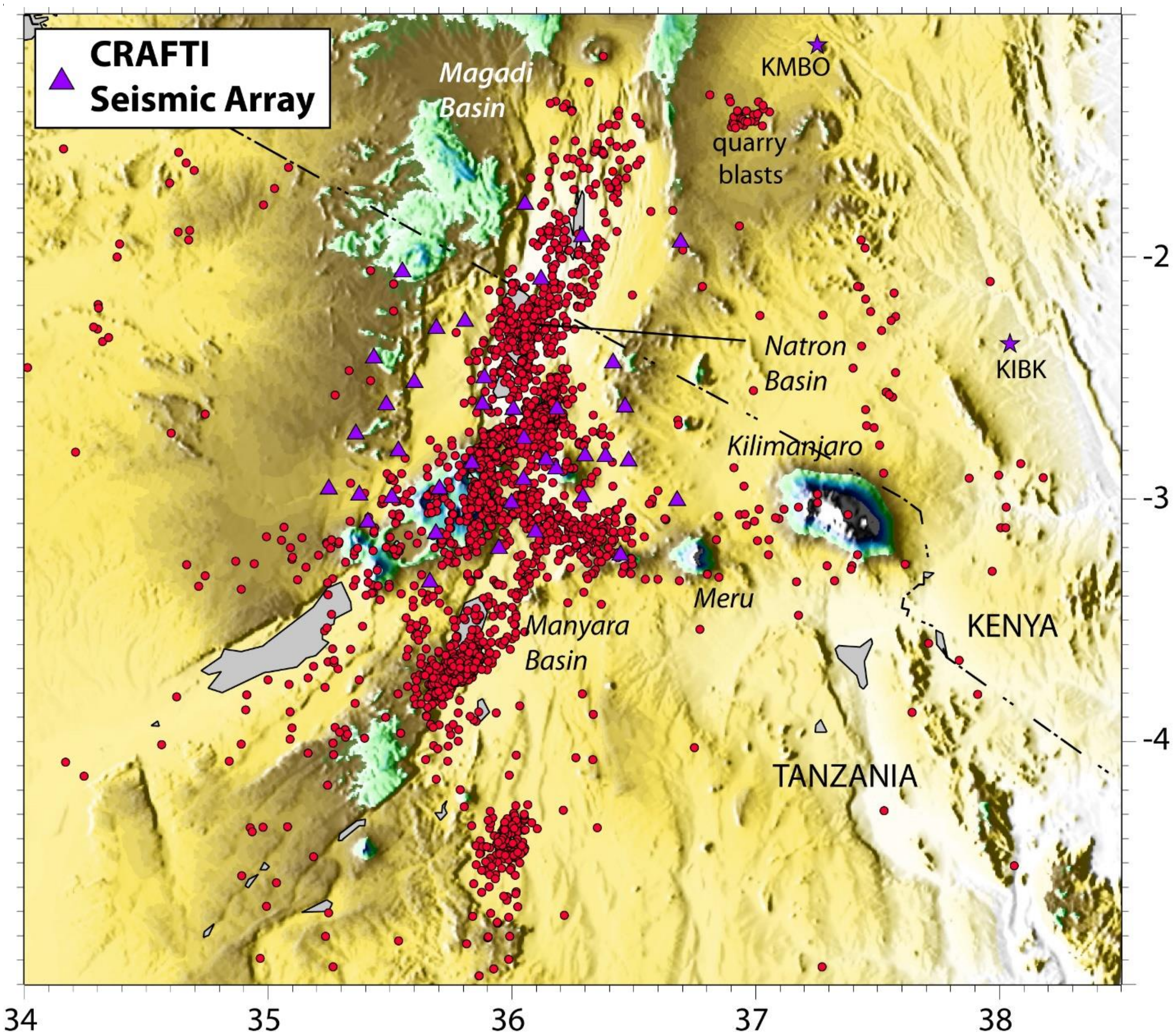

Figure S1 | CRAFTI seismic network (purple triangles) and GEOFON stations KIBK and KMBO also used in event locations (red circles).

© 2016 Macmillan Publishers Limited. All rights reserved.

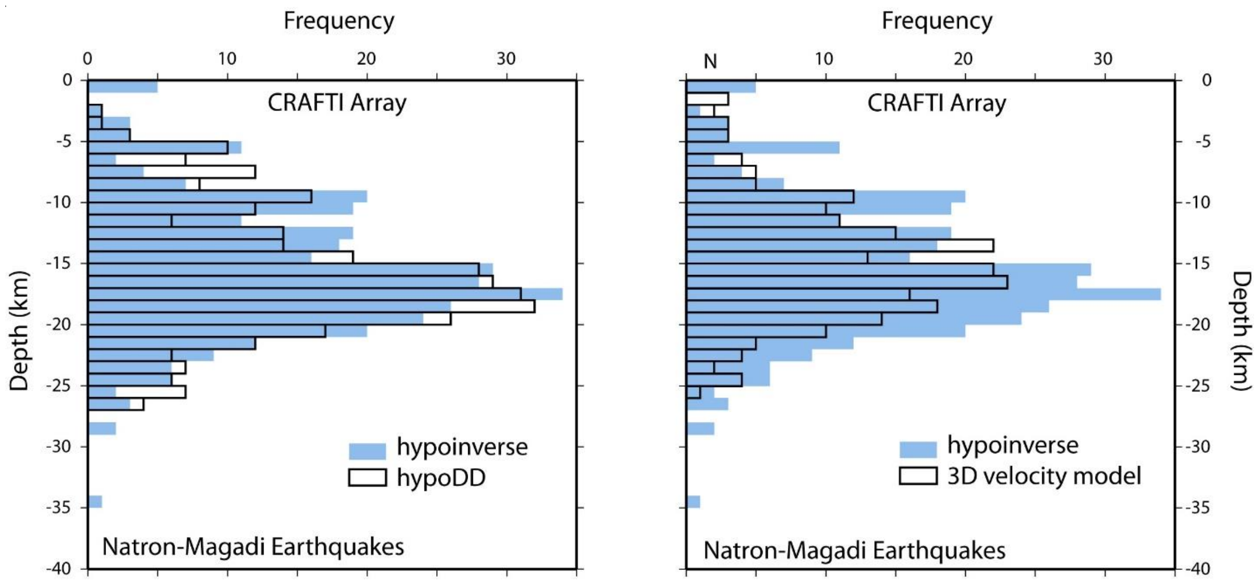

Figure S2 | Histograms comparing depths of CRAFTI earthquakes in the Natron and Magadi basins (excluding Gelai earthquakes). Earthquakes located using hypoinverse are compared to those relocated using the double-difference algorithm (left) and a sub-set relocated in the 3D tomographic inversion (right). The pattern of depth distributions show little variation between methods, demonstrating a significant set of earthquakes in the lower crust (15-27 km) along the length of the Natron and Magadi basins.

© 2016 Macmillan Publishers Limited. All rights reserved.

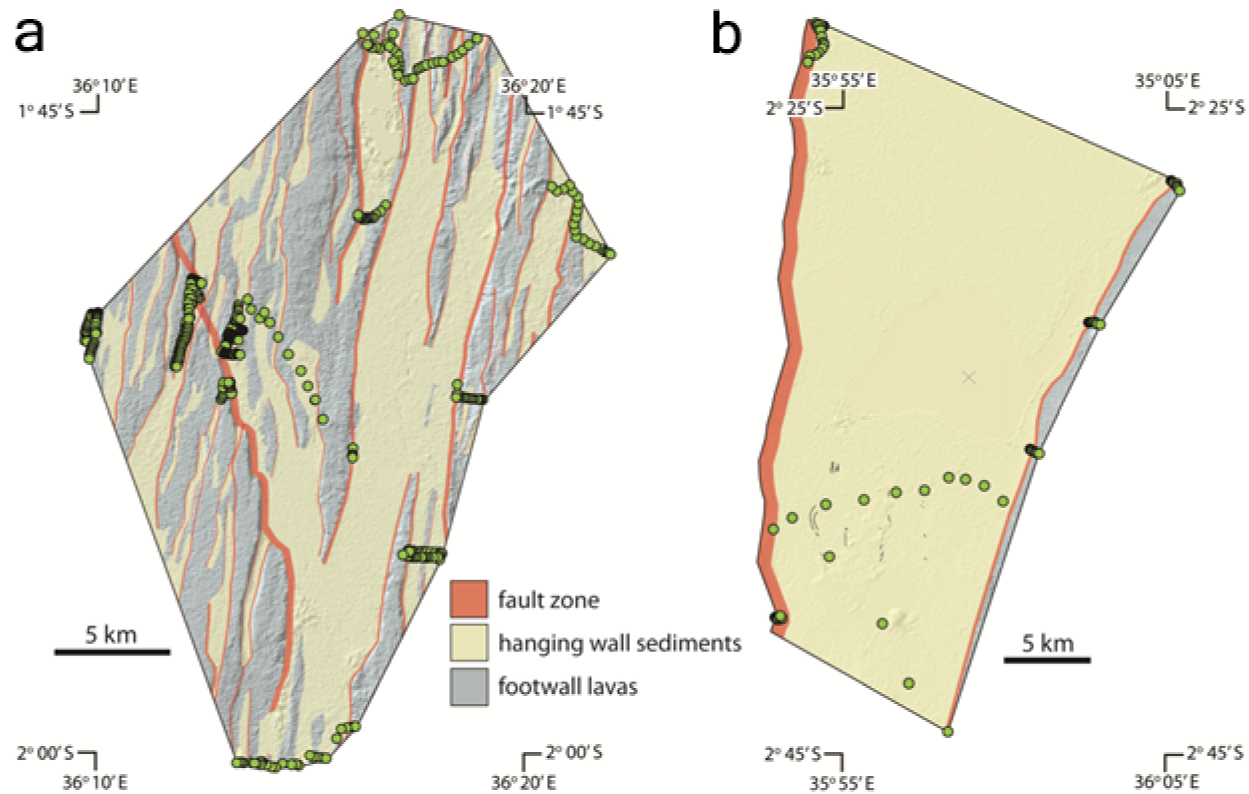

Figure S3 | Areal distributions of fault zones, hanging wall sediments, and footwall lavas in the Magadi (a) and Natron (b) basin study areas. Structural zones are overlain on an Aster GDEM v.2 hillshade. Locations of CO_2 flux measurements are presented as green circles. Small faults (10s to 100s of meters long) and short gaping fissures (10s of meters long) mapped in the field by ref. 34 are presented as black lines.

© 2016 Macmillan Publishers Limited. All rights reserved.

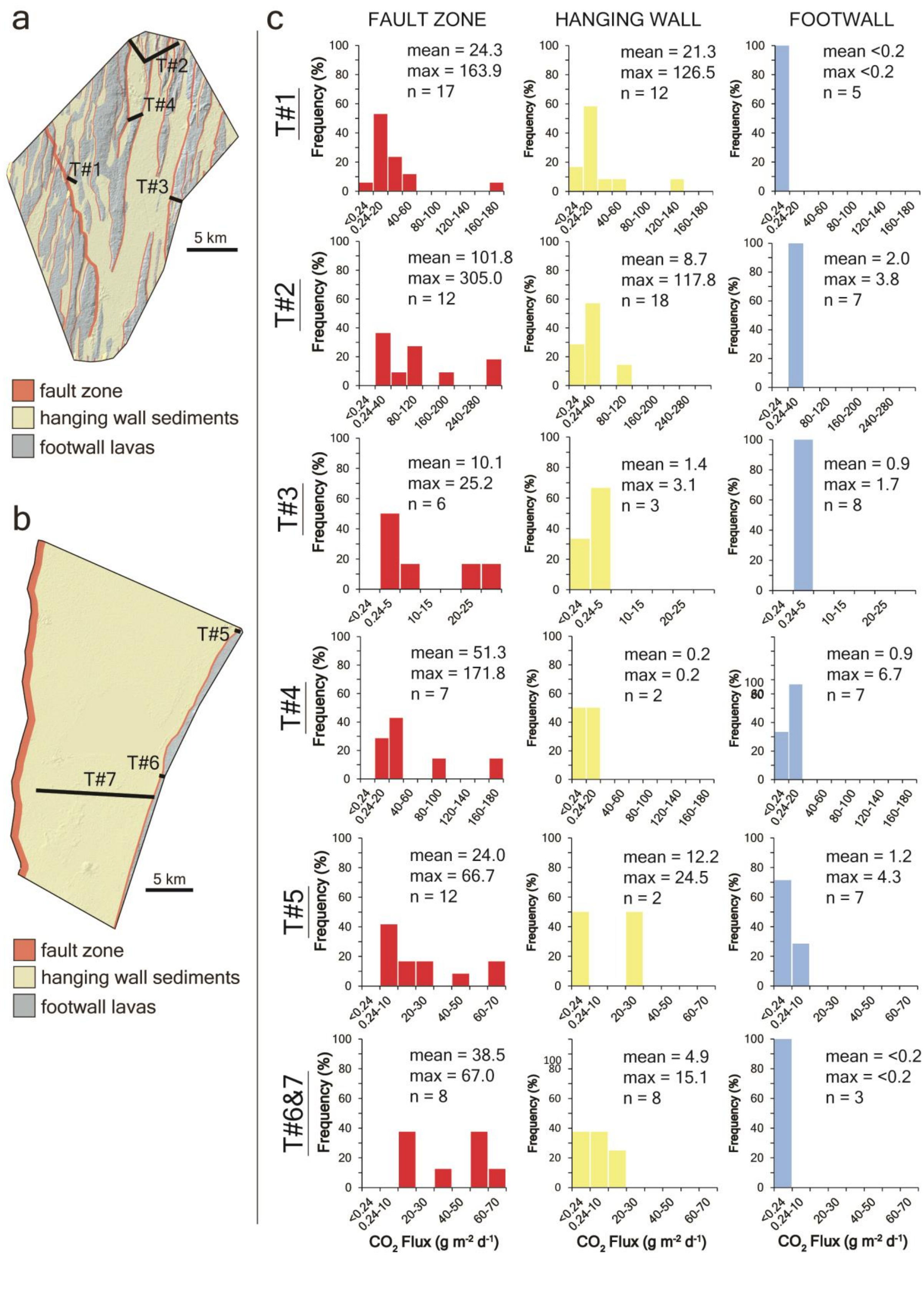

© 2016 Macmillan Publishers Limited. All rights reserved.

Figure S4 | Diffuse CO_2 flux data from 7 transects across the Natron-Magadi basin. **a,b**, general location of each transect in the Magadi (a) and Natron (b) study areas. Transect numbers (e.g., T#1, T#2) correspond to transect numbers of histograms in (c). Coordinates of study areas and sample locations are shown in Fig. S1. **c,** Histograms of diffuse CO_2 flux in fault zones (red), hanging walls (yellow), and footwalls (blue) from the transects shown in (a) and (b). Units for mean and max values are g m^{-2} d^{-1}.

© 2016 Macmillan Publishers Limited. All rights reserved.

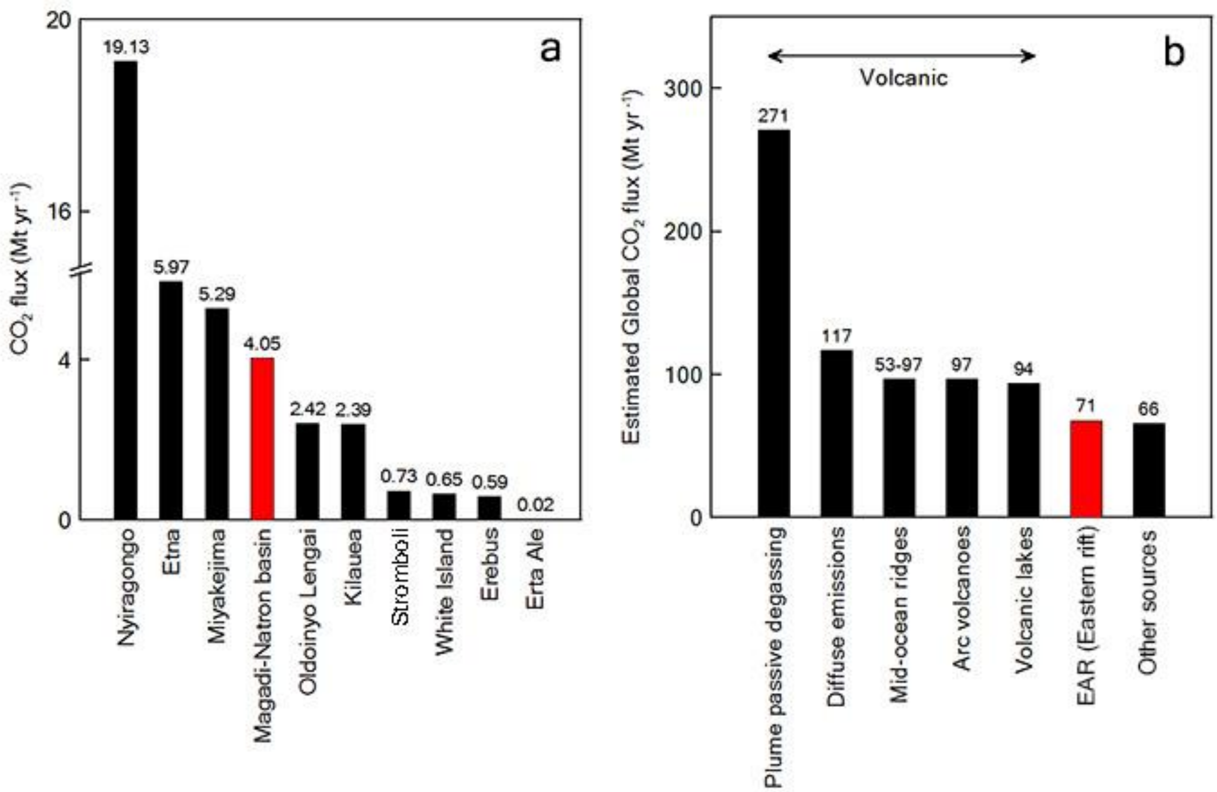

Figure S5 | Histograms of CO_2 flux. a. Annual CO_2 flux from tectonic degassing in the Magadi-Natron basin and a selection of volcanoes worldwide[1]. **b.** CO_2 flux from tectonic degassing in the EAR (Eastern rift) compared with global estimates from volcanoes and other sources (tectonic, hydrothermal, or inactive volcanic)[1, 35-37].

© 2016 Macmillan Publishers Limited. All rights reserved.

Table S1. Locations, gas compositions, C isotope values, and structural divisions of measured samples from the Magadi and Natron basin study areas and Oldoinyo Lengai North Crater.

Area	sample ID	location		Ar	N_2	O_2	CO_2	He	H_2	CH_4	CO	$\delta^{13}C$-CO_2	structural
		latitude (S°)	Longitude (E°)		vol. %				ppm			‰ vs. PDB	division
	A1P44	1.828625	36.167317	0.70	83.19	16.02	944.42	6.84	8.26	b.d.	b.d.	-8.5	FZ
	A1P63	1.84275	36.165028	0.70	83.28	15.94	832.00	7.11	5.45	b.d.	b.d.	-9.2	FZ
	A1P43	1.828289	36.167503	0.85	82.27	16.79	824.71	2.21	6.14	b.d.	16.03	-7.7	FZ
	A1P39	1.829833	36.165639	0.71	83.64	15.56	863.52	7.23	5.47	b.d.	b.d.	-9.6	HW
	A1P67	1.845944	36.164417	0.67	78.47	20.78	800.38	7.44	5.63	b.d.	b.d.	-8.7	FZ
	A2P82	1.838444	36.200167	0.66	80.61	18.66	642.53	6.49	5.35	b.d.	b.d.	-8.1	FZ
	A2P76	1.843972	36.198778	0.69	81.51	17.74	645.68	6.82	9.16	b.d.	16.32	-8.0	FZ
	A2P69	1.848028	36.1975	0.68	80.45	18.78	869.88	6.60	6.07	b.d.	b.d.	-10.1	FZ
	A2P86	1.834333	36.201639	0.66	80.85	18.42	688.76	7.29	5.62	b.d.	b.d.	-7.8	FW
	A3P5	1.859028	36.216361	0.76	78.94	20.22	803.95	0.96	5.86	b.d.	b.d.	-8.4	FZ
	A3P13	1.8575	36.218989	0.70	82.03	17.15	1223.27	9.21	4.26	b.d.	b.d.	-9.1	FZ
	A3P9	1.856528	36.216472	0.81	76.97	22.15	698.69	1.49	5.40	b.d.	b.d.	-9.9	HW
	A3P18	1.859328	36.219308	0.59	79.38	19.84	1882.03	13.47	4.37	b.d.	b.d.	-7.6	FZ
	A3P8	1.856833	36.216667	0.70	81.43	17.81	544.99	10.88	8.60	b.d.	b.d.	-7.2	FZ
	A3P21	1.85575	36.218472	0.70	83.55	15.36	3803.59	7.51	6.70	b.d.	b.d.	-7.9	FZ
Magadi	A4P27	1.835535	36.21852	0.86	82.60	16.46	768.65	1.47	4.57	b.d.	b.d.	-8.5	FZ
	A4P94	1.834439	36.222847	0.66	80.38	18.86	994.93	5.74	8.15	b.d.	15.77	-7.5	HW
	A4P82	1.844181	36.219661	0.86	82.32	16.70	1201.33	1.41	13.01	b.d.	b.d.	-7.1	HW
	A4P101	1.834103	36.220825	0.68	80.96	18.23	1314.96	6.61	6.58	b.d.	b.d.	-7.3	HW
	A4P111	1.836356	36.219469	0.82	81.82	17.31	578.11	7.43	6.45	b.d.	b.d.	-7.3	HW
	A4P113	1.8369	36.220089	0.71	80.05	19.14	990.99	7.67	6.11	b.d.	b.d.	-7.1	HW
	A4P81	1.844089	36.219269	0.65	81.23	17.99	1223.57	6.45	12.23	b.d.	18.19	-6.5	HW
	A4P90	1.844239	36.222794	0.68	82.28	16.95	919.84	5.70	8.27	b.d.	b.d.	-7.5	FZ
	A4P99	1.834244	36.221225	0.81	80.60	18.49	1025.56	2.30	5.75	b.d.	b.d.	-7.4	HW
	A4P108	1.835656	36.218458	0.82	80.51	18.62	464.87	10.02	4.94	b.d.	b.d.	-7.9	FZ
	A4P115	1.837517	36.220681	0.70	81.67	17.53	988.54	7.20	6.40	b.d.	b.d.	-5.9	HW
	A4P120	1.838653	36.221867	0.69	82.52	16.68	1053.10	11.22	4.88	b.d.	b.d.	-7.5	FZ
	A5P19	1.815472	36.205722	0.79	79.51	19.65	520.77	8.36	6.44	b.d.	b.d.	-8.3	HW
	A5P24	1.816417	36.207694	0.68	82.31	16.91	958.17	10.92	3.74	b.d.	b.d.	-7.8	FZ
	A5P34	1.824361	36.203278	0.69	80.32	18.91	835.54	9.20	9.12	b.d.	11.93	-8.6	HW
	A5P21	1.815889	36.2065	0.79	82.61	16.53	663.78	8.99	4.47	b.d.	b.d.	-7.4	HW

© 2016 Macmillan Publishers Limited. All rights reserved.

	A6P54	1.830889	36.22075	0.61	79.55	19.77	710.90	13.86	4.32	b.d.	b.d.	-8.0	FZ
	A6P50	1.829417	36.221194	0.67	80.95	18.29	873.04	6.04	5.84	b.d.	13.99	-11.1	FZ
	A6P52	1.831139	36.220667	0.69	82.27	16.89	1360.76	7.29	10.39	b.d.	b.d.	-6.5	FZ
	A7P30	1.921111	36.288222	0.74	82.89	16.29	784.68	11.22	9.06	b.d.	10.48	-5.8	HW
	A7P26	1.922417	36.288417	0.80	80.20	18.94	617.14	13.02	4.59	b.d.	b.d.	-10.2	HW
	A7P14	1.922694	36.3	1.08	80.64	18.22	573.68	8.71	5.69	b.d.	b.d.	-7.4	FZ
	A7P4	1.920306	36.289306	0.71	80.22	18.99	759.74	9.05	9.89	b.d.	b.d.	-6.4	HW
	A7P22	1.922611	36.292944	0.70	80.63	18.58	915.98	6.14	7.09	b.d.	15.99	-7.7	FW
	A7P12	1.921056	36.300694	0.68	80.72	18.51	881.32	6.31	17.93	b.d.	16.64	-8.9	FZ
	A7P5	1.920361	36.292444	0.83	82.34	16.78	484.60	7.68	7.52	b.d.	13.83	-7.1	HW
	A7P19	1.922639	36.294639	0.71	82.14	17.07	834.17	7.29	6.63	b.d.	16.45	-6.7	FZ
	A7P11	1.920778	36.300111	0.67	81.11	18.13	818.68	6.94	6.21	b.d.	b.d.	-6.9	HW
	A7P8	1.920528	36.294722	0.69	82.46	16.79	543.74	7.94	5.11	b.d.	b.d.	-8.1	FZ
	A7P29	1.922139	36.28775	0.86	82.56	16.51	659.63	9.54	4.19	b.d.	b.d.	-7.6	FZ
	A8P35	1.988944	36.264167	0.69	82.05	17.19	686.65	10.77	4.64	b.d.	b.d.	-6.2	FZ
	A8P40	2.000389	36.25275	0.72	81.21	17.97	969.67	8.67	12.59	b.d.	b.d.	-7	HW
	A8P50	2.00225	36.231458	0.68	82.23	16.98	1021.22	7.66	11.89	b.d.	b.d.	-7.3	FZ
	A8P42	1.999722	36.249889	0.67	82.17	17.09	662.11	6.05	7.51	b.d.	b.d.	-8.5	HW
	A9P9	1.730319	36.298964	0.70	82.11	17.11	842.79	6.70	6.90	b.d.	17.19	-9.3	FZ
	A9P5	1.732603	36.291972	0.86	81.06	18.03	497.51	2.31	8.45	b.d.	b.d.	-9.6	HW
	A9P4	1.733103	36.291111	0.67	81.21	18.05	676.82	5.91	6.32	b.d.	15.89	-8.6	HW
	A11P36	1.789639	36.268178	0.94	82.83	16.05	1735.20	2.00	9.37	b.d.	19.63	-5.7	FZ
	A11P29	1.791111	36.271242	0.66	82.73	16.53	776.27	12.62	6.91	b.d.	b.d.	-4.3	FZ
	A11P32	1.790764	36.269622	0.69	82.19	17.01	1107.14	9.93	5.06	b.d.	14.95	-3.8	FZ
	A11P22	1.785847	36.278933	0.69	81.18	18.05	779.67	8.95	5.99	b.d.	15.39	-9.1	FW
	A12P7	1.801833	36.359917	0.85	83.54	15.56	527.89	2.15	7.77	b.d.	b.d.	-9.3	HW
	A12P4	1.804222	36.364472	0.84	80.77	18.32	618.92	1.47	9.79	b.d.	18.57	-6.8	HW
	A12P17	1.780528	36.351111	0.85	80.56	18.52	666.84	1.66	5.89	b.d.	b.d.	-9.3	HW
	A12P9	1.799083	36.355278	0.70	82.78	16.43	822.19	7.42	6.65	b.d.	15.84	-8.5	HW
	A12P19	1.779556	36.347639	0.78	80.08	19.05	893.78	0.84	5.58	b.d.	16.00	-6.9	HW
	A12P1	1.802944	36.362472	0.71	82.26	16.98	487.25	7.25	7.51	b.d.	b.d.	-9.8	HW
	A13P38	1.855694	36.30675	0.87	82.01	17.01	1106.85	2.09	10.20	b.d.	b.d.	-7.4	FZ
	A13P37	1.860667	36.306194	0.85	82.04	17.00	981.63	9.35	10.16	b.d.	b.d.	-9.3	FZ
	A13P31	1.860861	36.309583	0.69	82.00	17.24	687.88	7.39	6.63	b.d.	18.52	-8.1	HW
	A14P6	1.734694	36.283478	0.68	81.40	17.81	1103.97	7.41	8.97	b.d.	19.51	-6.3	FZ
	A14P20	1.723619	36.271606	0.67	80.63	18.58	1107.60	6.94	5.47	b.d.	b.d.	-7.3	FZ
	A14P18	1.724681	36.273306	0.68	80.81	18.34	1647.35	7.41	5.82	b.d.	16.39	-6.5	FZ

© 2016 Macmillan Publishers Limited. All rights reserved.

	A14P7	1.735419	36.283494	0.65	77.72	21.51	1202.78	6.02	6.74	b.d.	b.d.	-8.3	FZ
	A14P10	1.730081	36.281619	0.69	81.60	17.49	2058.20	6.80	6.23	b.d.	16.86	-8.6	FZ
	A14P21	1.719167	36.269775	0.85	80.44	18.56	1420.52	32.71	10.04	b.d.	17.82	-8.9	FZ
	A14P1	1.727233	36.283283	0.68	80.96	18.28	787.91	6.45	5.72	b.d.	b.d.	-9.6	FW
	A14P4	1.731719	36.283842	0.68	82.13	17.11	771.18	5.77	11.76	b.d.	b.d.	-9.1	HW
	T1P1	2.373139	35.905806	0.67	81.78	17.47	773.14	8.26	5.42	b.d.	0.00	-9.3	FZ
	T1P2	2.373083	35.905278	0.69	82.51	16.69	1068.13	7.57	6.23	b.d.	14.40	-7.5	FZ
	T1P5	2.372639	35.904167	0.74	84.09	15.08	872.89	8.48	7.14	b.d.	24.81	-7.8	FZ
	T1P12	2.375583	35.904111	0.73	83.41	15.78	779.56	8.27	9.96	b.d.	20.67	-7.9	FZ
	T1P18	2.385	35.905194	0.73	83.83	15.34	988.28	8.04	5.96	b.d.	0.00	-8.8	FZ
	T1P23	2.392278	35.898278	0.73	84.07	15.12	879.30	7.98	6.49	b.d.	0.00	-8.3	FZ
	T3P12	2.679528	35.882139	0.72	83.73	15.46	807.21	7.87	10.21	b.d.	0.00	-7.5	FZ
	T3P13	2.6795	35.882389	0.70	83.83	15.38	882.85	7.37	6.17	b.d.	16.22	-8.1	FZ
	T3P14	2.6795	35.882722	0.72	81.05	18.13	961.39	6.20	6.24	b.d.	18.98	-7.9	FZ
	T3P17	2.679833	35.882667	0.76	83.66	15.49	872.08	7.40	6.11	b.d.	15.45	-8.0	FZ
	T3P22	2.680667	35.882889	0.70	81.08	18.15	699.21	6.90	11.90	b.d.	0.00	-7.7	FZ
	T3P26	2.680694	35.884056	0.71	83.61	15.56	1183.75	7.05	5.76	b.d.	0.00	-9.9	FZ
	T3P28	2.680657	35.884472	0.72	80.80	18.38	865.70	7.09	5.55	b.d.	0.00	-9.8	FZ
	T3P34	2.679583	35.8855	0.61	83.67	15.66	683.20	7.73	6.55	b.d.	0.00	-7.7	FZ
	T3P35	2.678889	35.88525	0.68	82.19	17.02	1033.39	7.66	9.76	b.d.	15.90	-10.6	FZ
Natron	T5P45	2.767	36.044861									-11.7	HW
	T6P7	2.453806	36.086861	0.85	77.64	21.39	1214.85	5.82	8.35	b.d.	21.70	-6.4	FZ
	T6P9	2.453944	36.087556	0.81	81.12	17.97	908.40	8.30	5.94	b.d.	0.00	-7.4	FZ
	T6P3	2.453556	36.086111	0.82	81.65	17.44	922.00	7.89	5.80	b.d.	0.00	-7.7	FZ
	T6P6	2.453778	36.086611	0.80	79.00	20.06	1414.51	7.18	6.25	b.d.	0.00	-7.2	FZ
	T6P11	2.453889	36.088278	0.84	80.19	18.87	1034.56	8.78	7.39	b.d.	16.76	-7.8	FZ
	T6P2	2.453	36.085944	0.86	83.62	15.43	879.47	13.15	11.22	b.d.	19.29	-8.6	HW
	T6P13	2.45425	36.088667	0.83	79.15	19.93	872.40	9.54	9.50	b.d.	0.00	-8.7	FZ
	T6P16	2.454972	36.088806	0.88	83.85	15.19	829.02	9.58	12.10	b.d.	14.96	-8.7	FW
	T7P27	2.526639	36.045278	0.85	81.60	17.33	1012.82	9.62	10.44	1250.03	0.00	-6.2	FZ
	T7P31	2.5265	36.046583	0.88	82.90	16.14	795.65	9.74	6.41	b.d.	15.62	-6.4	FZ
	T7P29	2.526083	36.046111	0.88	83.97	15.06	808.82	9.74	6.33	b.d.	22.35	-6.5	FZ
	T7P24	2.526639	36.044278	0.81	82.33	16.76	957.88	9.78	10.15	b.d.	0.00	-7.7	FZ
	T7P22	2.526361	36.043667	0.84	83.75	15.31	995.48	9.32	11.58	b.d.	18.75	-8.8	FZ
	T7P23	2.526389	36.043972	0.87	83.36	15.68	888.45	9.57	9.78	b.d.	0.00	-8.7	FZ
	T7P35	2.527333	36.049278	0.87	83.75	15.29	762.89	9.52	10.10	b.d.	19.22	-8.1	FW

© 2016 Macmillan Publishers Limited. All rights reserved.

	T8P42	2.59325	36.015889	0.90	81.56	17.44	925.20	10.26	6.20	b.d.	15.73	-7.8	FZ
	T8P36	2.592333	36.014194	0.92	83.52	15.43	1224.22	10.44	6.37	b.d.	0.00	-8.2	FZ
	T8P38	2.592472	36.014778	0.84	79.33	19.74	853.63	9.65	5.44	b.d.	0.00	-8.6	FZ
	T8P40	2.592889	36.015333	0.93	83.36	15.60	1072.86	11.80	5.72	b.d.	0.00	-9.1	FZ
	T9P47	2.610667	35.989583	0.87	83.67	15.37	887.28	10.64	6.16	b.d.	19.08	-9.1	HW
	T9P49	2.606694	35.971306	0.83	82.24	16.86	669.92	9.44	5.91	b.d.	0.00	-10.6	HW
	T9P52	2.618306	35.927556	0.64	77.08	22.19	788.17	6.82	6.94	b.d.	15.86	-9.8	HW
	T9P53	2.620972	35.908028	0.69	83.42	15.78	1040.75	7.79	6.72	b.d.	16.62	-9.7	HW
Oldoinyo Lengai North Crater	OL21	2.761513	35.91533									-5.7	
	OL23	2.761339	35.915594	0.83	83.16	15.14	8655.19	9.82	6.49	b.d.	21.48	-3.0	
	OL24	2.761322	35.915638	0.83	83.16	15.29	7091.05	9.79	12.26	b.d.	20.51	-2.2	

FZ: fault zone. HW: hanging wall. FW: footwall. **b.d.: below detection limit.** No gas chemistry data for T5P45 and OL21.

© 2016 Macmillan Publishers Limited. All rights reserved.

Table S2. Diffuse CO_2 flux data (in g m^{-2} d^{-1}) for different structural zones in the Magadi and Natron basin study areas.

	Magadi basin			Natron basin		
	fault zone	hanging wall	footwall	fault zone	hanging wall	footwall
number of data	174	186	93	71	24	17
mean flux	36.6	8.8	1.9	17.2	11.7	1.1
error (95% conf.)	11	2.6	1.4	5	6.8	0.8

© 2016 Macmillan Publishers Limited. All rights reserved.

Table S3: Summary of diffuse CO_2 flux for the Magadi-Natron basin, including mean and total flux from different structural zones, and estimated annual flux from each study area.

study area	structural zone	mean flux ($g\ m^{-2}d^{-1}$)	area (km^2)	total flux ($g\ d^{-1}$)	annual flux ($Mt\ yr^{-1}$)
Magadi	fault zones	36.6 ± 11.0	72.9	2.7×10^9	0.98 ± 0.29
	hanging walls	8.8 ± 2.6	150.7	1.3×10^9	0.48 ± 0.14
	footwalls	1.9 ± 1.4	183.8	3.5×10^8	0.13 ± 0.10
	total		407.5		1.59 ± 0.53
Natron	fault zones	17.2 ± 5.0	33.1	5.7×10^8	0.21 ± 0.06
	hanging walls	11.7 ± 6.8	526.5	6.2×10^9	2.25 ± 1.31
	footwalls	1.1 ± 0.8	14.4	1.6×10^7	< 0.01
	total		574		2.46 ± 1.37

Mean and annual flux values are within 95% confidence

© 2016 Macmillan Publishers Limited. All rights reserved.

Table S4: Locations, temperatures, and pH of springs in the Magadi-Natron basin.

	ID	latitude (S°)	longitude (E°)	Temperature (℃)	pH
Magadi	KN14-S01	1.85744	36.21900	48.4	8.9
	KN14-S02	1.86319	36.21983	47.7	9.3
	KN14-S03	1.83581	36.21839	46.4	9.1
	KN14-S04	1.84329	36.21583	34.1	-
	KN14-S05	2.00228	36.23148	44.7	9.8
	KN14-S06	1.99825	36.23131	44.6	9.9
	KN14-S07	2.00284	36.22848	39	9.8
	KN14-S08	1.72756	36.28086	83.5	9.5
	KN14-S09	1.72547	36.27828	82.3	9.3
	KN14-S10	1.72461	36.27308	-	-
	KN14-S11	1.85989	36.30636	35	10
Natron	TZ14-S01	2.37314	35.90581	50.7	10.3
	TZ14-S02	2.39228	35.89828	51.2	10.3
	TZ14-S03	2.45581	36.08842	43.1	9.5
	TZ14-S04	2.52733	36.04928	-	-
	TZ14-S05	2.52733	36.04928	38.1	9.3
	TZ14-S06	2.59283	36.01597	36.8	9.2

© 2016 Macmillan Publishers Limited. All rights reserved.

Supplementary References

1. Burton, M. R., Sawyer, G. M. & Granieri, D. Deep carbon emission from volcanoes. *Rev. Mineral. Geochem.* **75**, 323-354 (2013).
2. Chiodini, G., Cardellini, C., Amato, A., Boschi, E., Caliro, S., Frondini, F. & Ventura, G. Carbon dioxide Earth degassing and seismogenesis in central and southern Italy. *Geophys. Res. Lett.* **31** (2004).
3. Jolie, E., Klinkmueller, M. & Moeck, I. Diffuse surface emanations as indicator of structural permeability in fault-controlled geothermal systems. *J. Volcanol. Geotherm. Res.* **290**, 97-113 (2015).
4. Crossley, R. The Cenozoic stratigraphy and structure of the western part of the Rift Valley in southern Kenya. *J. Geol. Soc. London* **139,** 393-405 (1979).
5. Angelier, J. Bergerat, F., Dauteuil, O. & Villemin, T. Effective tension-shear relationships in extensional fissure swarms, axial rift zone of northeastern Iceland. *J. Struct. Geol.* **19**, 673–685 (1997).
6. Grant, J. V. & Kattenhorn, S. A. Evolution of vertical faults at an extensional plate boundary, southwest Iceland. *J. Struct. Geol.* **26**, 537–57 (2004).
7. Cowie, P. A., Scholz, C., Edwards, M. & Malinverno, A. Fault strain and seismic coupling on mid-ocean ridges. *J. Geophys. Res.* **98**, 17911-17920 (1993).
8. Chiodini, G. *et al.* Carbon isotopic composition of soil CO_2 efflux, a powerful method to discriminate different sources feeding soil CO_2 degassing in volcanic hydrothermal areas. *Earth Planet. Sci. Lett.* **274**, 372–379 (2008).

© 2016 Macmillan Publishers Limited. All rights reserved.

9. Werner, C. & Cardellini, C. Comparison of carbon dioxide emissions with fluid upflow, chemistry, and geologic structures at the Rotorua geothermal system, New Zealand. *Geothermics* **35**, 221–238 (2006).

10. Deutsch, C. V. & Journel, A. G. *GSLIB: Geostatistical software library and users guide* (Oxford Univ. Press, New York, 1998).

11. Foster, A., Ebinger, C., Mbede, E. & Rex, D. Tectonic development of the northern Tanzanian sector of the east African rift system. *J. Geol. Soc.* **154**, 689–700 (1997).

12. Morner, N. A. & Etiope, G. Carbon degassing from the lithosphere. *Glob. Planet. Change*, **33**. 185–203 (2002).

13. Ebinger, C. J. & Scholz, C. A. Continental Rift Basins: The East African Perspective. in *Tectonics of sedimentary basins: recent advances Ch. 9* (eds. Busby, C. & Azor, A.) (John Wiley & Sons, Chichester, UK, 2012).

14. Ibs-von Seht, M., Blumenstein, S., Wagner, R., Hollnack, D. & Wohlenberg, J. Seismicity, seismotectonics and crustal structure of the southern Kenya Rift – new data from the Lake Magadi area. *Geophys. J. Int.* **146**, 439–453 (2001).

15. Keir, D. *et al.* Lower crustal earthquakes near the Ethiopian rift induced by magmatic processes. *Geochem. Geophys. Geosyst*. **10**, Q0AB02 (2009).

16. Nyblade, A. A., Birt, C., Langston, C. A., Owens, T. J. & Last, R. J. Seismic experiment reveals rifting of the craton in Tanzania. *Eos* **77**, 517–521 (1996).

17. Hollnack, D. & Stangl, R. The seismicity related to the southern part of the Kenya rift. *J. Afr. Earth Sci.* **26**, 477–495 (1998).

© 2016 Macmillan Publishers Limited. All rights reserved.

18. Keir, D., Ebinger, C. J., Stuart, G. W., Daly, E. & Ayele, A. Strain accommodation by magmatism and faulting as rifting proceeds to breakup: seismicity of the northern Ethiopian rift. *J. Geophys. Res.* **111,** B05314 (2006).

19. Belachew, M. *et al.* Comparison of dike intrusions in an incipient seafloor-spreading segment of Afar, Ethiopia: seismicity perspectives. *J. Geophys. Res.* **116**, B06405 (2011).

20. Birt, C. S. et al. The influence of pre-existing structures on the evolution of the southern Kenya rift valley – Evidence from seismic and gravity studies. *Tectonophysics* **278**, 211–242 (1997).

21. Calais, E. *et al*. Aseismic strain accommodation by slow slip and dyking in a youthful continental rift, East Africa. *Nature* **456** (2008).

22. Keller, G. R., Mechie, J., Braile, L.W., Mooney, W. D. & Prodehl, C. Seismic structure of the uppermost mantle beneath the Kenya rift. *Tectonophysics* **236**, 201–216 (1994).

23. Keranen, K., Klempere, S. & Gloaguen, R. EAGLE Working Group, Three dimensional seismic imaging of a proto-ridge axis in the Main Ethiopian Rift, *Geology* **39**, 949–952 (2004).

24. Lindenfeld, M., Rumpker, G., Link, K., Koehn, D. & Batte, A. Fluid-triggered earthquake swarms in the Rwenzori region, East African Rift - evidence for rift initiation. *Tectonophysics* **566**, 95-104 (2012).

25. Reyners, M., Eberhart-Phillips, D. & Stuart, G. The role of fluids in lower-crustal earthquakes near continental rifts. *Nature* **446**, 1075–1079 (2007).

26. Geissler, W. H. Seismic structure and location of a CO_2 source in the upper mantle of the western Eger (Ohře) rift, central Europe. *Tectonics* **24**, TC5001 (2005).

© 2016 Macmillan Publishers Limited. All rights reserved.

27. Kendall, J. -M., Stuart, G. W., Ebinger, C. J., Bastow, I. D. & Keir, D. Magma-assisted rifting in Ethiopia, *Nature* **433**, 146–148 (2004).

28. Whaler, K. & Hautot, S. The electrical resistivity structure of the crust beneath the northern Ethiopian rift. *Geol. Soc. Spec. Publ*. **256,** 294–305 (2006).

29. Keir, D. *et al*. Mapping the evolving strain field during continental breakup from crustal anisotropy in the Afar Depression. *Nature Communications* **2**, 285 (2011).

30. Biggs, J., Amelung, F., Gourmelen, N., Dixon, T. H. & Kim, S. W. InSAR observations of 2007 Tanzania rifting episode reveal mixed fault and dyke extension in an immature continental rift. *Geophys. J. Int.* **179**, 549–558 (2009).

31. Kennedy, B. M. *et al.* Mantle fluids in the San Andreas fault system, California. *Science* **278**, 1278–1281 (1997).

32. Albaric, J., Déverchère, J., Perrot, J., Jakovlev, A. & Deschamps, A. Deep crustal earthquakes in North Tanzania, East Africa: interplay between tectonic and magmatic processes in an incipient rift. *Geochem. Geophys. Geosyst.* **15**, 374–394 (2014).

33. Mulibo, G. & Nyblade, A.The 1994–1995 Manyara and Kwamtoro earthquake swarms: variation in the depth extent of seismicity in northern Tanzania. *S. Afr. J. Geol.* **112**, 387-404 (2009).

34. Sherrod, D. R., Magigita, M. M. & Kwelwa, S. Geologic map of Oldonyo Lengai (Oldoinyo Lengai) volcano and surroundings, Arusha region, *United Republic of Tanzania. Tech. Rep. 2013-1306, U.S. Geol. Surv.* pp. 65 (2013).

35. Marty, B. & Tolstikhin, I. N. CO_2 fluxes from mid-ocean ridges, arcs and plumes. *Chem. Geol.* **145**, 233–248 (1998).

36. Kagoshima, T. *et al.* Sulphur geodynamic cycle. *Sci. Rep*. **5**, 8330 (2015).

© 2016 Macmillan Publishers Limited. All rights reserved.

37. Pérez, N. M. *et al.* Global CO_2 emission from volcanic lakes. *Geology* **39**, 235–238 (2011).

© 2016 Macmillan Publishers Limited. All rights reserved.